NEUROSCIENCE

Spatially controlled, bipolar, cortical stimulation with high-capacitance, mechanically flexible subdural surface microelectrode arrays

Ilke Uguz and Kenneth L. Shepard*

Most neuromodulation approaches rely on extracellular electrical stimulation with penetrating electrodes at the cost of cortical damage. Surface electrodes, in contrast, are much less invasive but are challenged by the lack of proximity to axonal processes, leading to poor resolution. Here, we demonstrate that high-density (40-μm pitch), high-capacitance (>1 nF), single neuronal resolution PEDOT:PSS electrodes can be programmed to shape the charge injection front selectively at depths approaching 300 micrometers with a lateral resolution better than 100 micrometers. These electrodes, patterned on thin-film parylene substrate, can be subdurally implanted and adhere to the pial surface in chronic settings. By leveraging surface arrays that are optically transparent with PEDOT:PSS local interconnects and integrated with depth electrodes, we are able to combine surface stimulation and recording with calcium imaging and depth recording to demonstrate these spatial limits of bidirectional communication with pyramidal neurons in mouse visual cortex both laterally and at depth from the surface.

INTRODUCTION

High-resolution bidirectional communication with neural populations is critical for building functionally targeted brain-machine interfaces (*1*, *2*). Electrical stimulation–based neuromodulation is the basis for the actuation of brain function, but targeting electrical stimulation selectively to key functional domains within the cortex remains challenging. Visual prosthetics are one example, in which electrical stimulation of the visual cortex has been shown to be an effective tool for the generation of visual percepts called phosphenes (*3*, *4*). In this application, spatiotemporal precision of stimulation is key to actuating specific sensory outputs, such as orientation, direction of motion, and color. Improving the spatial selectivity of such sensory modulations in a minimally invasive manner requires microscale, high-density electrode sites and particular electrode stimulation configurations.

Electrical stimulation is often characterized by electrode current values in the range of microamperes to milliamperes; stimulation is generally biphasic but monopolar. In this case, it has been shown that the current density inside the brain shows a circular distribution around the electrode that exponentially decays as a function of distance (*5*, *6*). Early cortical stimulation models estimated that cell bodies that overlap within the radius of stimulation would be activated and the field of effect would be directly determined by current amplitude. However, more extensive work combining electrical stimulation with high spatial modalities such as two-photon (2p) imaging and functional magnetic resonance imaging has since showed that this high spatial control is not possible since a larger network of neurons are depolarized transsynaptically (*7*–*9*). It is well established that sodium channels are mainly concentrated in axonal segments (*10*) with electrical stimulation widely viewed to be through these axonal terminals (*7*). As a result, stimulation causes a sparse response at antidromically activated cell bodies that can be more distant from the electrode tip. To minimize this sparsity during monopolar microstimulation, most approaches rely on penetrating electrodes (*11*–*13*) to achieve the closest possible proximity of electrodes with axons. This way, only the axons that are in the immediate vicinity of the probes can be activated, and postsynaptic somatic propagation will be in a smaller volume. However, the use of penetrating electrode technologies results in tissue damage. The insertion injury triggers an inflammatory response, leading to glial scarring around the implanted electrodes and resulting in the formation of insulating layer between the brain and the electrodes (*14*, *15*). This decreases not only for the recorded signal quality but also for the stimulation efficacy because of the presence of a layer of dead tissue that must be breached to reach healthy neurons. In addition, especially with rigid implants, micromotion of the brain prevents electrodes from successfully stimulating the same neuronal groups repeatedly in chronic settings.

An alternative to this approach is to use electrocorticography (ECoG) devices to deliver the stimulation pulses from the surface of the brain to the deeper cortical layers. Integration of ECoG arrays with flexible thin-film materials has already been shown to achieve neural coupling without any influence on the tissue integrity on the superficial layers of the brain (*16*–*18*). Studies show, however, that superficial stimulation requires current values orders of magnitudes higher than intracortical studies because of the enhanced distance to the axons of the pyramidal neurons (*19*, *20*). This corresponds to current levels that exceed the charge injection capacity of traditional capacitive metal electrodes when fabricated at the microscale. Clinical macroelectrodes to breach this constraint are designed at millimeter dimensions and lack spatial resolution as a result (*21*). In addition, the increased distance to the neurons of interest results in a much larger activation area compare to penetrating electrodes. Here, we seek to investigate the degree to which high-capacitance microelectrodes can be used along with bipolar stimulation to achieve localized, vertically tunable stimulation profiles. In bipolar stimulation, the proximity of the source and sink electrodes are chosen to further shape the electrical response. This is in contrast to unipolar stimulation in which current is sunk at a distant counter-electrode. We also demonstrate that the stimulated sodium spikes can be recorded by the same surface electrodes. For single pyramidal neuron, these

Department of Electrical Engineering, Columbia University, New York, NY, USA.
*Corresponding author. Email: shepard@ee.columbia.edu

can be at depths up to 160 μm below the pial surface, while for groups of pyramidal neurons, surface recording can capture activity at depths of up to 270 μm.

All of this is accomplished with a thin-film multielectrode array (MEA) composed of conducting polymer [poly(3,4-ethylenedioxythiophene):poly(styrenesulfonate) (PEDOT:PSS)] electrodes patterned at neuron-size density onto an ultrathin film (4-μm) parylene substrate. The soft and porous nature of the device allows it to form, in the case of chronic implantation, a very low-impedance connection to the pial surface of the cortex, allowing current injection in excess of 50 μA to be achieved without reaching 1-V compliance levels. The MEAs are tuned to be optically transparent to allow concurrent calcium imaging for mapping immediate neural response to stimulation pulses at depth. This allows us to generate synaptic activation maps and to determine stimulation mechanisms. By combining surface and depth electrodes on the same substrate, we record somatic sodium spikes at the site of origin and track their projection to the surface. By applying the current in a bipolar configuration between adjacent microelectrodes on pitches of 40 μm or less, we demonstrate the ability to confine the current injection to a localized two-dimensional (2D) plane and achieve a lateral stimulation resolution of 80 to 100 μm in the mouse model for layer 2 (L2) and L3 neurons. The results of this work inform how emerging high-density capacitive surface electrode arrays can be used for targeted brain stimulation studies.

RESULTS

Potential fields induced by controlled bipolar stimulation in cortex

In this study, we focus on stimulation of V1 in the visual cortex of the mouse model, which contains functional columns that primarily consist of densely packed sets of pyramidal neurons that project down to L6 (*21*). Effective and focused manipulation of these functional groups requires delivery of currents several hundreds of micrometers inside the tissue in a localized fashion with densities in the range of nanoampere per square micrometer. To accomplish this, we use an array of PEDOT:PSS circular electrodes with a diameter of 15 μm and a pitch of 40 μm (Fig. 1A). This particular configuration has been shown to record neuronal activity from single neuronal scale to local field potentials (LFPs) with high signal-to-noise ratio (*16*). Therefore, we chose it as starting point of the stimulation experiments. Size and pitch of the electrodes are easily scalable on the basis of the application. The capacitance of the PEDOT:PSS electrodes scales linearly with the volume of the film (*22*). This high volumetric capacitance (39 F/cm^3) allows fabrication of microelectrodes that match the size of an individual neuron while maintaining capacitance in the range of nanofarads. We measure the 30-nm-thick PEDOT:PSS-coated gold electrodes to have an impedance value of 90 kilohms at 1 kHz (fig. S1, A and B).

We begin by characterizing the current distribution resulting from surface stimulation. To achieve effective charge injection, we laminate the flexible MEA on the pial surface of the brain, which, in our first experiments, is performed with removal of the skull and dura, with a micrometer-scale hole etched in the MEA in between stimulating electrode pairs (Fig. 1A). We insert a micromanipulator-driven patch pipette with an inner diameter of 500 nm and outer diameter of 2 μm vertically through this hole to measure the current density distribution inside the tissue during surface stimulation. Because a certain amount of tissue buckling occurs on pipette insertion, we start all measurements at 20 μm below the pial surface after the probe successfully penetrates the tissue.

To be able to get an accurate 2D map of charge density, for each stimulation pulse, we reposition the micropipette axially (by varying the depth of penetration) and, for each axial position, sequentially activate a selection of electrodes at various lateral positions as shown in Fig. 1A. For the stimulation protocol in all cases in this study, we use constant-current biphasic (cathodic and then anodic) 100 μs per phase square pulses with varying amplitudes starting from 32 μA and ramping up gradually to 60 μA (*23*, *24*). Pulse durations that exceed the chronaxie of neurons (30 to 200 μs for axons) produce tissue damage and increase the stimulation thresholds (*25*). The time between pulses is kept at 2 ms, larger than the refractory period of induced somatic activity. Each pulse is charge-balanced to avoid net oxidation or reduction of the electrode material (Fig. 1B). We perform these measurements with both unipolar and bipolar stimulation. In the former, the stimulating electrode applies current pulses with respect to a stainless steel counter-electrode that is placed in the cerebellum. In the latter, we configure the electrodes surrounding the stimulation electrode to apply pulses of opposite polarity, but equal amplitude (in total), to fully sink the lateral current. We plot the peak measured current density induced by these stimulation patterns in Fig. 1B (see Materials and Methods). The tissue is not perfectly homogenous, with variations in glial and neuronal cell composition and vascular structures. To compensate for this, we average five sets of experiments at different positions to obtain more homogeneous current density profiles.

For both the unipolar and bipolar configurations, the initial measurements performed right after implantation show that the majority of the measured current is shunted on the brain surface (Fig. 1B). The removal of the dura causes the release of cerebrospinal fluid (CSF), providing a high conductance path between electrodes and preventing substantial current from entering the cortex. We find that the ability to stimulate at depth improves significantly if the arrays are instead implanted chronically and subdurally (Fig. 1C). Instead of removing the dura completely, we perform an incision that is large enough for lateral insertion of the MEA under the dura. In this case, the micrometer-scale holes in between the electrode pairs help to minimize the disruption to CSF transport (Fig. 1A). We cover the surgery area with gel foam and a coverslip and keep the device implanted for 7 days, allowing the tissue to heal around the array. Coronal section of the subdural implant site in chronic configuration show damage only at the dura incision site after 1 month. Around the electrode area, minimal reactive tissue and fibrosis is observed (fig. S2).

To measure the current distribution in this configuration, we now insert the pipettes through the intact dura matter. For unipolar stimulation, we obtain a uniform semicircular charge-density distribution propagating from the point-source electrode that decreases exponentially as a function of distance from the electrode. The potentials measured in this case penetrate much deeper into the tissue (Fig. 1D) than those performed with dura removal. Measurements performed 100 μm below the pial surface for 10 separate implantations show average current density levels on the order of 3 nA/μm^2 for subdural implantation, whereas the yield to reach same current density levels in the case of dura removal at the same depth is only 30% (Fig. 1E).

L1 constitutes the most superficial layer of the visual cortex with a depth in the range of 100 to 120 μm and consists of distal apical

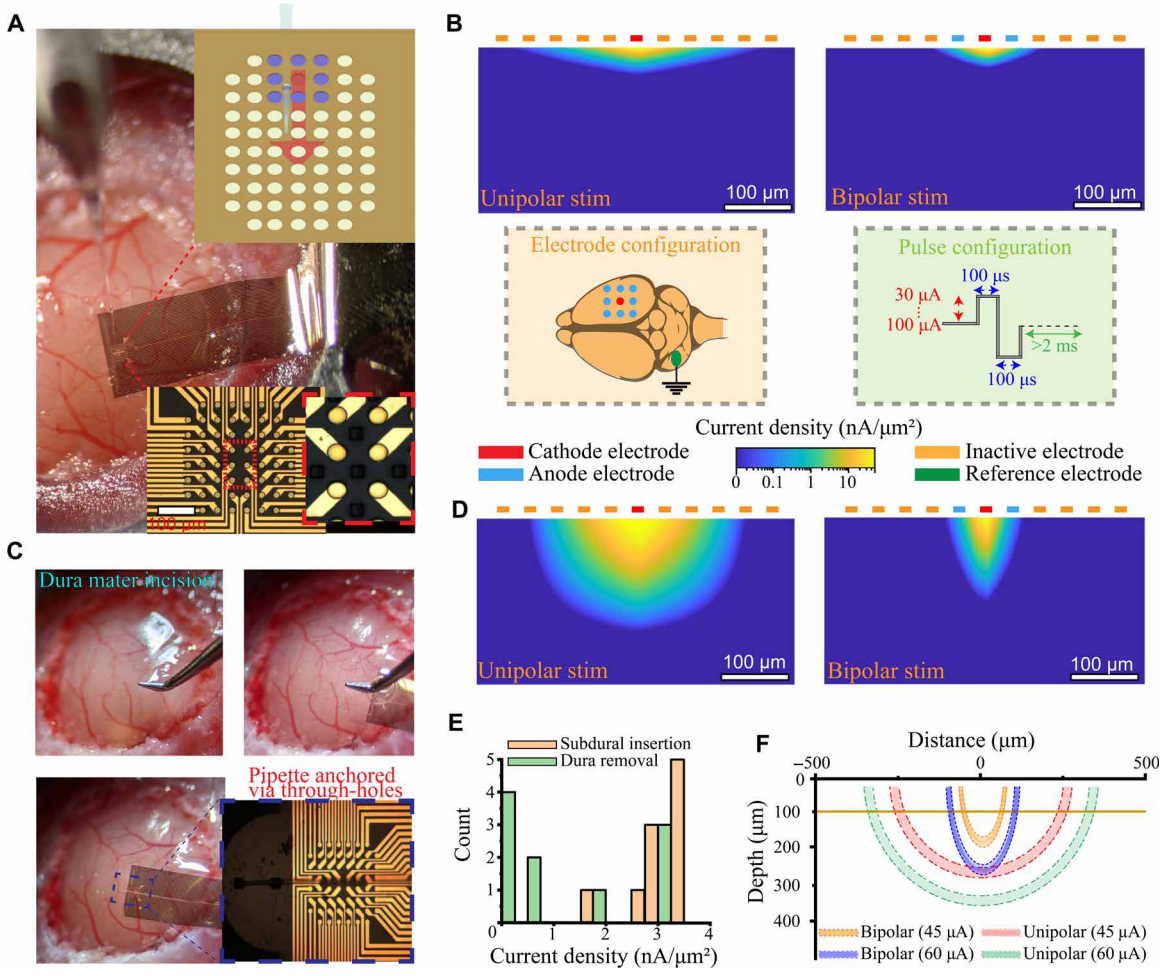

Fig. 1. Current distribution inside the brain for various stimulation configurations with surface MEAs. (**A**) Micropipette insertion through the laminated array on the exposed surface of the brain. The inset shows an illustration of the electrode layout as viewed from the top side (15-µm-diameter electrodes with a 40-µm pitch). A pipette is inserted at depths from 20 to 500 µm, and stimulated electrodes are shifted as shown by the arrow for each insertion step. (**B**) Postimplantation current distribution inside the brain with dura removal immediately after implantation. Measurements start 20 µm below the pial surface. Inset of the figure shows the stimulation configuration. Bottom left inset illustrates the placement of cathodic and anodic electrodes on the visual cortex and reference electrode in the cerebellum. Bottom right inset illustrates the structure of the applied stimulation pulses. (**C**) Subdural device implantation. First, the dura mater is incised using a dura hook. The surface MEA, anchored to a carrier glass pipette, is positioned under the dura matter. The carrier pipette is retracted to leave the active area of the MEA implanted on the surface of the brain under the intact dura mater. (**D**) Post-subdural implantation current distribution inside the brain in chronic setting. (**E**) Histogram shows how many times associated current density is obtained at a depth of 100 µm in the brain in the case of acute implantation with dura removal (green) and in the case of chronic implantation with an intact dura (orange). (**F**) Estimated limits of maximum stimulation distance from surface microelectrodes located at position (0, 0) for both bipolar and unipolar stimulation paradigm. The yellow line is plotted to illustrate the depth of L2 neurons in the mouse model.

dendrites coming from pyramidal neurons located in deeper layers. The axons of local pyramidal neurons, on the other hand, rarely extend toward L1, suggesting that they are less likely to be directly activated with superficial current inputs (*23*). Direct stimulation of L2 and L3 axonal structures requires augmentation of the effective field of stimulation with larger applied currents. For unipolar stimulation, this results in the loss of lateral spatial control. However, with bipolar stimulation, the charge injection is tightly confined between adjacent electrodes (Fig. 1D). Some loss in the depth of penetration results from directing the current return to the adjacent electrode, but this can be compensated by increasing the injected current.

During unipolar stimulation with implanted depth electrodes, the relationship between the current amplitude (I) and the radius (r) of directly activated tissue is given by $I = Kr^2$, where K, the current-distance constant, indicates the amount of current required to directly activate neural tissue 1 mm away from the electrode tip (*6*). In practice, there is wide variation in this constant resulting from differences in orientation, thickness, and myelination of axons in the stimulated tissue. For cortical pyramidal cells, K is measured to be 1292 µA/mm^2 (*6*), which corresponds to a current density of 100 pA/µm^2 at the outer contour of a stimulated region. Using this current density threshold value to define the maximum limit of stimulation for current amplitudes of both 45 and 60 µA for both unipolar and bipolar stimulation, the maximum laterally and axially extent of stimulation can be determined as shown in Fig. 1F. With bipolar stimulation, this stimulation extent reaches into L2, the depth of which is noted in Fig. 1F, while keeping the stimulation thresholds at the surface to a radius of less than 100 µm, which is approximately

equal to the sum of the electrode spacing and diameter. We now seek to validate these regions of stimulation at depth by incorporating surface electrodes with two recording modalities; simultaneous 2p imaging of calcium indicators and depth probes implanted right under the stimulation electrode pairs.

Simultaneous stimulation and functional optical imaging to characterize stimulation thresholds

Observation of the immediate electrophysiological neural response from surface recording electrodes is difficult because of high post-stimulation artifacts. In addition, spiking responses from individual neurons have magnitudes in the range of only a few microvolts and do not travel large distances. Instead, we combine surface electrical stimulation capabilities with 2p imaging of calcium indicators. In particular, we use transgenic GCAMP6f animals with the vesicular glutamate transporter 1 (VGlut1) promoter, showing dense expression in the entire cortical volume and fast calcium dynamics. We image L2/L3 of V1 in head-fixed mice while stimulating in the same area.

To obtain an imaging window under the active stimulation area, we fabricate an array substituting gold interconnects with optically transparent PEDOT:PSS in the active area with a length of 400 μm. The capacitance of PEDOT:PSS films and therefore their charge injection capacity increases linearly with film thickness, while film transparency is inversely proportional to both thickness and capacitance (fig. S3A). A film thickness of 100 nm is chosen as a balance between this optical transparency and electrode capacitance. PEDOT:PSS has a much lower electrical conductivity compared to metals, since insulating PSS-rich shells encapsulate conducting PEDOT rich domains (300 S/cm), although it can be increased significantly (to 652 S/cm) by treatment with concentrated H_2SO_4, which removes the excess PSS and leads to the formation of a crystallized structure (*24*). 2p imaging through these arrays is possible at depths in excess of 500 μm at laser powers on the order of 30 mW. The resultant microelectrodes with a diameter of 15 μm have an impedance value of 130 kilohms at 1 kHz with a capacitance of 1.2 nF (fig. S3B), a value comparable to the PEDOT:PSS-coated metal electrodes in Fig. 1 (90 kilohms). To enable bipolar stimulation, we fashion these electrodes in pairs with a single circular electrode (with a diameter of 15 μm) surrounded by a ring electrode (inner diameter of 65 μm and output diameter of 75 μm as shown in Fig. 2A). The ring electrode configuration allows increasing transparency and spatial coverage while maximizing the number of active sites. The current density distribution during stimulation with ring electrodes follows closely that of the electrode geometry of Fig. 1A at the same electrode spacing of 25 μm (fig. S4), allowing us to connect the experiments performed with the two different configurations.

To analyze the long-term durability of the transparent electrodes, we implant the arrays and configure each set of electrodes to apply pulses at different amplitudes. We find that the transparent electrodes have a lifetime that drops below 500 cycles for current values above 100 μA (fig. S5). We therefore limit the amplitude of stimulation to 60 μA for the concurrent in vivo imaging experiments. At these current limits, scanning electron microscopy (SEM) examination of the electrodes shows no damage after 1000 cycles (fig. S6).

To avoid the suppression at synapses due to anesthesia, all the in vivo experiments are done with awake animals. Recorded fluorescence changes are the sum of individual action potentials. Single spikes lead to intracellular Ca_2^+ increases with time-to-peak ~8 ms after excitation and slow decay times on the order of 100 ms from the overlapping transients of individual spikes. Spike signals sit atop large background fluorescence transients, requiring accurate deconvolution for spike reconstruction (*25*). Because our primary aim is to determine which neurons are activated at the time of stimulation, we focus on the rise time of each calcium transient and observe how it aligns with the stimulation pulses as a determinant of stimulation threshold. By configuring the 2p microscope in resonance mode and acquiring the data at high frame rates (30 Hz), we precisely resolve the rising phase of the somatic response during the stimulation pulse train. Neuronal expression varies from animal to animal, and parameters such as laser power or photomultiplier gain were recalibrated with each experiment. To be able to achieve a standard baseline, we calculated $\Delta F/F$ for each measurement and defined 25% as the threshold for event detection. All the calcium transients were analyzed, and spike detection was performed using the Suite2p pipeline (*26*).

To study activation mechanisms at depth in response to surface stimulation, we can classify the type of neuronal activity detected by 2p microscopy as deriving from either somatic or neuropil activity. Neuropils are primarily the submicrometer-scale neuron components that are not resolved by the 2p microscope such as dendrites, axons, and other neuronal processes. When cortical synapses are blocked using the glutamate antagonist GYKI53655, the neuropil activation remains largely unaltered, while cell body activation is eliminated (*27*). This suggests that the observed neuropil activity in the cortex is primarily presynaptic with minimal contributions from somatic activity. Because of this, we use neuropil response as a proxy for measuring current spread during electrical stimulation, while we use somatic spike activation to measure the post-stimulation synaptic propagation (*8*).

We first examined neuropil response that correlated with stimulation pulses at various amplitudes. An example of a representative 2p image at a depth of 120 μm below the pial surface, corresponding to L2, is shown in Fig. 2A. The neuropil activity stimulated by three bipolar stimulation electrode pairs that are sequentially activated is projected onto the color map in Fig. 2B. An example of raw traces to generate these maps is plotted in fig. S7A. At a stimulation magnitude of 45 μA for bipolar stimulation with electrode spacing of 25 μm, the strongest response is observed around the inner electrode and shows an exponential decay as a function of distance (0.0064 ± 0.001 mm^2 for 0.25 $\Delta F/F$), which is consistent with the measured current distribution in Fig. 1D. Increasing the amplitude to 60 μA results in an increase in the affected area at a depth of 120 μm to 0.0136 ± 0.00192 mm^2 for 0.25 $\Delta F/F$. To map the extent of stimulation on L2/L3 neurons, we show these same results at six different depths from 40 to 350 μm with response to stimulation amplitude of 60 μA in Fig. 2C. Neuropil response in layer 1 is relatively weak. We believe that this is due to low axonal concentration on the surface of the brain and indirect stimulation of dendrites via axonal propagation. On L2/L3, where the highest axonal input density is observed on the other hand, neuropil response shows perfect overlap with the current density measurements in Fig. 1D. A response (0.2 $\Delta F/F$) is still observable as deep as 280 μm, whereas the response fully diminishes at 320 μm. In contrast, for unipolar stimulation at 60-μA amplitude of the center electrode, neuropils as deep as 320 μm are activated (Fig. 2C) but with a poor lateral confinement. Lower unipolar stimulation amplitude (45 μA) shows smaller response yet still with high sparsity (fig. S7B). The observed activation profile

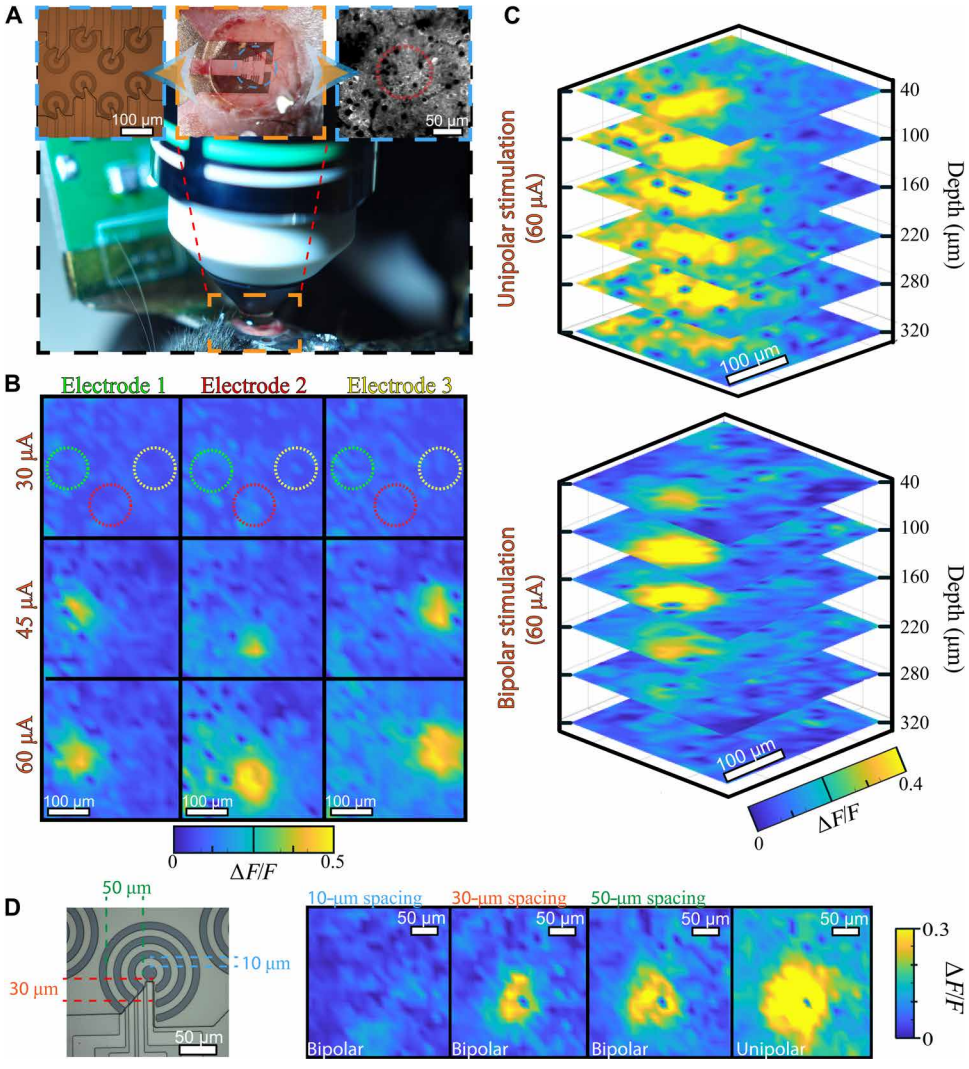

Fig. 2. Spatial distribution of neuropil response to superficial electrical stimulation for unipolar and bipolar configurations. (**A**) Experimental setup for combined electrophysiology and 2p imaging. Mice are head-fixed to the imaging setup with a metallic headplate. A ×16 immersion objective is used to acquire 2p images. The flexible electrode array is connected to backend electronics that is anchored to the side of the headplate. Top left: Micrograph of the stimulating transparent array with cathode electrode surrounded by anode electrodes with a spacing of 25 μm. Top middle: Image of the cranial window with the implanted array that is sealed by a coverslip to form the imaging window. Top right: Image of the cortical surface with 2p microscopy through an electrode pair marked by red circle. (**B**) Neuropil response as a function of stimulation current for bipolar stimulation with an electrode spacing of 25 μm. Green, red, and yellow circles on the top color maps represents the positions of three different outer ring electrodes. Each color map shows a planar stimulation response at 100 μm below the pial surface for each electrode pair for 30-, 45-, and 60-μA stimulation currents. (**C**) Color maps show stacked vertical slices due to stimulation from a single electrode for a current pulse of 60 μA acquired at various depths below the pial surface for unipolar (top) and bipolar (bottom) configurations. (**D**) A micrograph of multiring electrode structure. Color maps on the right side show neuropil response to a stimulation current of 60 μA, starting from inner sink stimulation electrode to outer ones. The last map is for unipolar stimulation.

for both modalities shows a high correspondence to the current distribution obtained with same current parameters in Fig. 1D.

To investigate the effects of anode-cathode spacing on the locality of bipolar stimulation, we fabricate electrodes with the multiring structure shown in Fig. 2G. In each case, we use the center electrode as cathode and surrounding ring electrodes with varying pitches as anode. At the closest spacing (10 μm), we do not observe a neuropil response because conduction finds a shallow path at these spacings. For 30- and 50-μm spacings, however, a response profile is apparent as shown in Fig. 2G. In both cases, the neuropil activation is limited to inside the zone defined by the anode electrodes. The lateral extent of the neuropil stimulation can be tightly controlled in this manner with bipolar stimulation. In a dense MEA structure, this allows a wide range of options for the shape and scale of spatial confinement.

To characterize the somatic calcium spikes, we determine the firing probability of responsive somas as a function of applied bipolar simulation at a depth of 100 μm in Fig. 3A. Effective synchronization of fluorescent somatic activity to stimulation onset is only observed when the pulse amplitude reaches at least 45 μA; a representative somatic response that is fully synchronized to 60-μA stimulation pulses is shown in Fig. 3B. Additional examples of somatic response during stimulation with 45- and 100-μA pulses are illustrated in fig. S7C. Longer spike transients are observed over 100-μA pulses

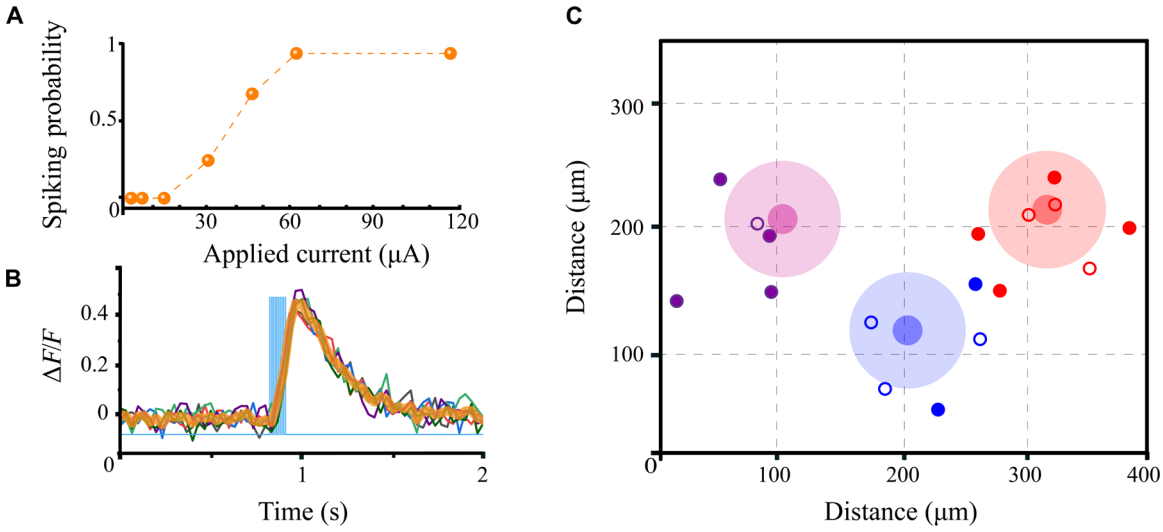

Fig. 3. Spatial and temporal characteristics of somatic responses to superficial electrical stimulation for bipolar configurations. (**A**) Spiking probability of responsive somas as a function of applied current obtained from five animals and 17 somas. (**B**) Fluorescence traces of a single responsive soma to 60-μA pulses. Each of six repetitions is plotted in a single color, and the mean is plotted in orange. Blue traces represent the stimulation pulse train. (**C**) Spatial somatic response distribution as a function of stimulation current acquired at three different electrode pairs marked as purple, red, and blue circles. Corresponding somatic traces are marked as the same color of stimulating electrode. Somas that are activated by both 45- and 60-μA amplitude currents are marked as empty circles, and somas activated only by 60-μA current amplitude are marked as filled circles.

because of induced bursting of somatic bodies at high current densities. To see the spatial distribution of somatic response in the imaging plane, we repeat the same experiment across a larger field of view (400 μm by 400 μm) containing three stimulation electrode pairs. In Fig. 3C, we plot the responsive L2 somas as a function of distance from each bipolar stimulating electrode pair. Despite the high density of somatic bodies within the field of stimulation, only a small fraction of them are activated because they likely project their axons outside the activation zone. At the same time, observed somatic response is reflective of those neurons, which do project axons into the stimulation zone. As a result, all the responsive somas were selectively activated by stimulation from the corresponding ring electrode and not from the adjacent ones. For an accurate comparison between different stimulation amplitudes and configuration, somatic activation tests are conducted in a single 2D plane. Taking into account an average somatic body size of 15 μm, we expect the number of activated neurons to be an order of magnitude higher around the activation zone defined at Figs. 1D and 2C. The average lateral extent of somatic bodies extends to a diameter of 100 μm for 45-μA amplitude and 130 μm for 60-μA amplitude, consistent with predictions in the analysis of Fig. 1D. The level of somatic activation locality is comparable to that from penetrating electrodes (*7*) and validates the anisotropic, laterally confined delivery of current to L2 neurons with bipolar surface electrodes.

Determining the possible contribution of apical dendrites to surface stimulation

While we have assumed that surface stimulation is mediated by axonal stimulation, it is useful to consider the possible role of apical dendrites. Dendritic tufts are in close proximity to the electrode surface, while activated somas and axonal hillocks are typically at L2/L3. Despite their high threshold of stimulation, it is possible that stimulation-induced transmembrane currents can be conducted intracellularly from the dendritic tree to the axon hillock and contribute to stimulation. To further investigate this potential dendritic stimulation mechanism, we design two separate stimulation experiments; in one, we block all superficial cortical input, while in the other, we selectively suppress the apical dendritic inputs on the surface by superficial release of inhibitory drugs. To achieve effective and local drug delivery, we use the through-holes between the cathode and anode as drug release sites. We seal the device after the implantation by using a coverslip integrated with a 20-μm poly(dimethylsiloxane) (PDMS) fluidic channel (*28*). The center of the fluidic channel overlaps the electrodes with an inlet and outlet in the coverslip (Fig. 4A). The channel is filled with artificial CSF and sealed to avoid leakage (Fig. 4A).

In the first set of experiments, we image responsive somatic spikes at L2 as high concentrations (50 mM) of 4-[([2H-benzopyran-2-one-7-amino-4-methoxy] carbonyl) amino] butanoic acid (GABA) are delivered through the fluidic channel. GABA is an inhibitory neurotransmitter that activates $GABA_A$ receptors and suppresses interictal activity (*29*). From Fick's law, the diffusive flux of GABA is given by $J = -D(dc/dx)$, where D is the GABA diffusion coefficient (0.36 um^2/ms) (*30*) and c is concentration. Using this equation, at a surface concentration of 50 mM, the concentration at a depth of 220 μm will reach 20 μM, sufficient to inhibit neuronal activity, in 250 s (*31*). Actual diffusion times will be longer because of uptake mechanisms for GABA and variations in the diffusion coefficient. Consistent with GABA delivery reaching the depth of imaging, after 300 s, we observe a decrease in the spontaneous firing of somas on the areas under the release sites (Fig. 4B). Although GABA concentration reaches threshold concentration over L1 dendrites within 100 s, we observe a decrease in the stimulation responses at the field of imaging only after 300 s (Fig. 4C). This suggests that the primary input of stimulation is within the plane of imaging and is not superficial.

In the second set of experiments that selectively suppress superficial dendritic input, we pharmacologically block hyperpolarization-activated cyclic nucleotide–gated (HCN) channels at the dendritic

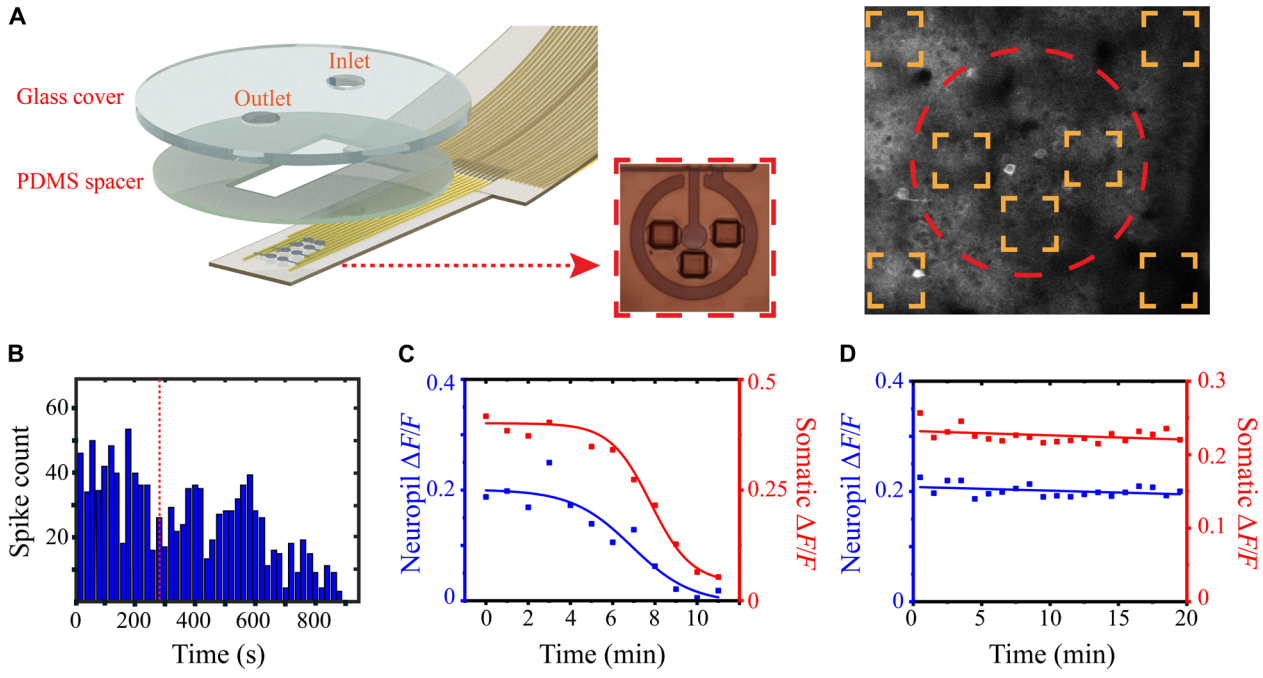

Fig. 4. Neuropil and somatic response to surface stimulation during axonal and dendritic inhibition during superficial delivery of neurotransmitters. (**A**) A depiction of the drug release platform. A coverslip integrated with a PDMS spacer is used to encapsulate the implanted array. Two holes are etched on the coverslip to be used as inlet and outlet for drug injection. In brackets is an image of single transparent stimulating electrodes with integrated drug release sites. On the right side is a micrograph of the acquired 2p image through the device. The electrode area is marked by a red circle (diameter, 150 μm), and drug release sites are marked as orange rectangles. (**B**) The spontaneous somatic firing rate is plotted as a function of time. The red dashed line represents the time of GABA release. (**C**) The plot shows the Δ*F*/*F* of somatic (marked as red) and neuropil (marked as blue) activity acquired at the time of stimulation as a function of time after GABA release. (**D**) The plot shows the Δ*F*/*F* of somatic (marked as red) and neuropil (marked as blue) activity acquired at the time of stimulation as a function of time after ZD7288 release.

tufts, which regulate the membrane potential and resting conductance of pyramidal neurons and control the integration of excitatory and inhibitory synaptic input (*32*). With superficial release of 4-ethylphenylamino-1,2-dimethyl-6-methylaminopyrimidinium chloride (ZD7288; 1 mM), an HCN channel blocker, we inhibit dendritic input selectively and observe its effects on our ability to stimulate action potential. Topical administration of ZD7288 on the brain surface has been shown to diffuse over millimeter range and effectively block off HCN channels within 15 min (*33*). Δ*F*/*F* recorded during stimulation for both neuropil and somatic activity at a depth of 120 μm does not show any substantial decay during ZD7288 delivery, ruling out contributions of dendritic stimulation to observed somatic activity (Fig. 4D).

Surface stimulation combined with electrical depth recording

While thin-film surface MEAs have demonstrated the ability to record single unit activity (SUA) and multiunit activity (MUA) from the surface of the brain, the neurophysiological origin of this spiking activity is still a subject of investigation. Combining surface recording of sodium spiking activity with surface stimulation provides an opportunity for bidirectional communications with pyramidal neurons. Despite offering high spatial resolution, 2p microscopy has difficulty capturing the fast dynamics of individual spikes. To supplement measurement of stimulation effects using optical microscopy, we also correlate surface stimulation with depth recording. The challenge in these measurements is the short distance the recording electrodes must be to the soma to detect Na_+ spikes on the order of 200 μm (*34*). As a result, accurate relative placement of the surface electrodes and depth electrodes is important. To that end, we fabricate a version of our μECoG array, shown in Fig. 5A, that incorporates an implantable probe on the same substrate. This implantable probe has a small pocket at its tip for attachment to a carrier shank for insertion. After implantation of the surface array, a carrier shank is used to insert the flexible extension, leaving the shank inside the cortex and the rest of the electrodes on the surface (Fig. 5A).

We repeat the successful stimulation parameters (60 μA, bipolar) used in the 2p experiments of Figs. 2 and 3, while recording the response on both the depth and surface electrodes. Although the recording amplifiers pick up stimulation artifacts (fig. S8), neuronal excitation is maintained after the stimulation period (*35*), allowing us to record spiking frequencies before and after the stimulation onset to detect the responsive cells. To detect SUA and MUA, we filter raw data between 300 Hz and 5 kHz, detecting spike clusters with Kilosort2 (*36*). Clusters exhibiting interspike interval histograms (fig. S9A) and autocorrelograms (fig. S9B) consistent with typical neuronal refractory periods (0 to 2 ms) are identified as representing SUA, while clusters with high refractory period violations are identified as resulting from MUA. Typical SUA and MUA recordings exhibit a range of spontaneous firing rates (0.1 to 0.5 Hz), which is increased to 2 to 9 Hz for SUA and 10 to 30 Hz for MUA post-stimulation at depths as much as 270 μm (Fig. 5B).

We also analyze the spatial decay of both stimulated and spontaneous somatic spikes recorded along the depth shank (Fig. 5C). Isolated putative units identified at depths up to 160 μm are cocaptured by the surface electrodes at attenuated amplitudes. These recorded

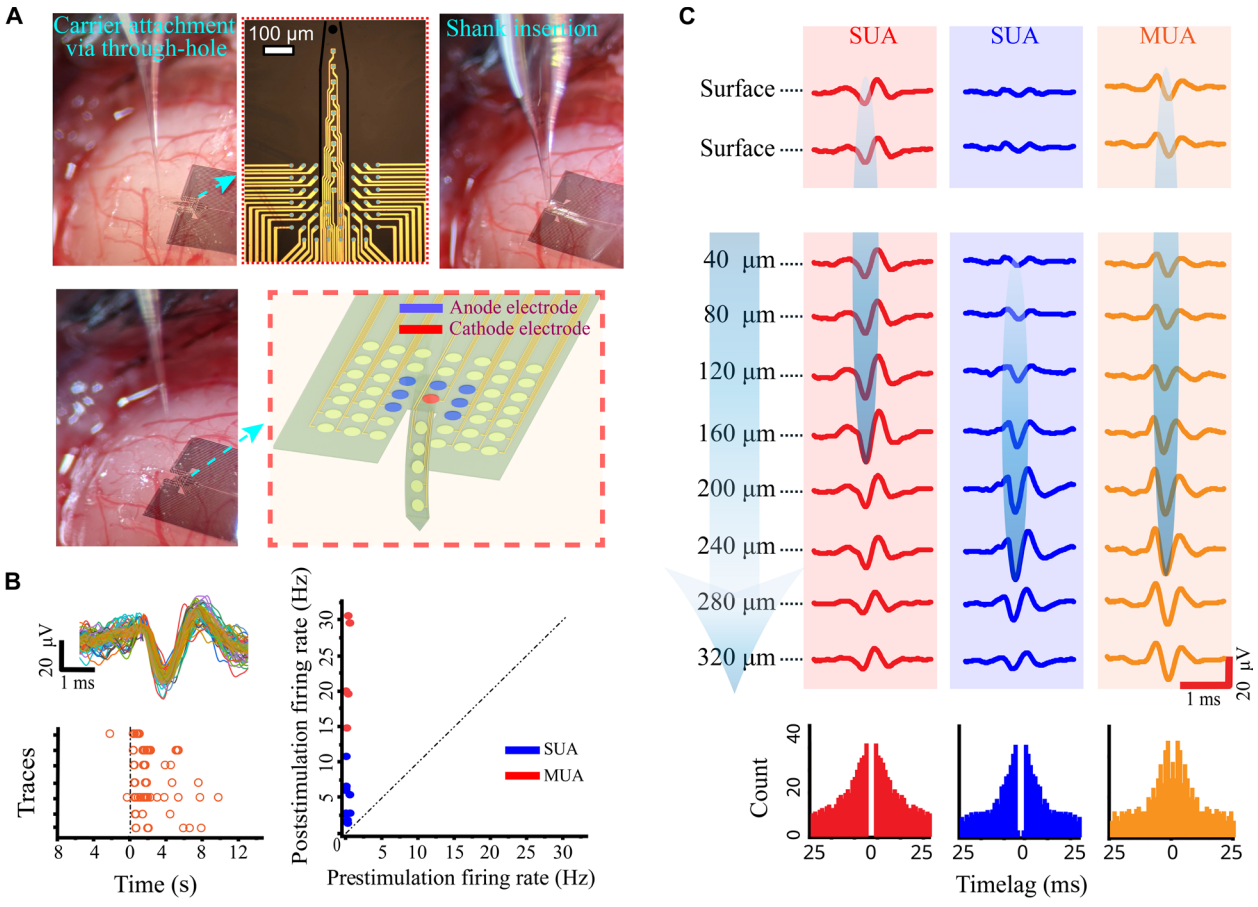

Fig. 5. Response of single and multineuronal activity during surface stimulation recorded at surface and depth by a 3D neural probe. (**A**) Implantation process of the dual surface and depth probe. The 3D array is laminated on the exposed surface of the brain. A carrier glass pipette is anchored to the shank extension with a through-hole. A pipette is subsequently used to insert the shank and retracted to leave the fully flexible dual probe inserted partially inside and partially on the surface of the brain. On the top center is a micrograph of the array. The shank extension has 10 electrodes reaching down to 500 μm below the pial surface. PEDOT:PSS electrodes are highlighted in blue. On the bottom right is an illustration of the implanted probe inside and on the surface of the brain. (B) Spike waveform obtained by averaging 50 traces that are acquired at 160 μm below the pial surface from a single soma. On the bottom left is an example of spike traces during stimulation pulses, marked in black. Right: Pre- and post-stimulation firing rate plot of responsive somatic spikes. SUA is marked as blue circles, and MUA is marked as red circles ($n = 5$). (**C**) Recorded voltage of spiking activity by various electrodes at the surface of the brain and at depth. Traces on the left side and center are acquired from single spikes, and traces on the right side are from multi-units. Corresponding autocorrelograms are shown in the bottom panel.

amplitudes at the surface are as low as 16 μV over a noise baseline of 4 μV across the 300-Hz to 5-kHz band. SUAs that were sourced at deeper regions (>200 μm) attenuate completely and are not captured by surface probes (Fig. 5C). In contrast, MUAs typically generate a much larger spatial response that is recorded by multiple depth and surface electrodes. MUAs recorded at the surface result primarily from simultaneous spiking activity of L2/L3 pyramidal cells with potential contributions from L1 interneurons and backward-propagating, dendritic spikes from deeper layers (*37*). We further confirm this with concurrent imaging and electrophysiology experiments using transparent microelectrodes implanted in V1 with visual stimulation (see Materials and Methods). We observe that synchronized populations of somatic bodies imaged by 2p microscopy can generate strong MUA responses on the surface electrodes (fig. S10). The ability to stimulate and detect those pyramidal neuron columns as deep as 270 μm will be key to the practical use of surface electrodes to achieve targeted recording and neuromodulation.

Effect of stimulation on LFPs

Other important components of the recorded electrophysiological activity in vivo are the LFPs, which reflect dendritic inputs generated by synchronized synaptic activity (*34*). Synchronous calcium and sodium potentials from many neurons can contribute substantially to high-frequency components of the LFP that can be quite local. For example, in the visual cortex, it has been shown that activity originating within 250 μm of a recording electrode can show substantial differences in domains as small as 100 μm (*38*). Therefore, valuable information can be extracted from the LFP about the spatial activity of local neuronal populations that respond to stimulation.

We first analyze the change in power spectra of recorded LFPs before and after stimulation as recorded by the shank electrodes during biphasic stimulation pulses at amplitudes of 60 and 100 μA. At the larger surface stimulation amplitude up to 100 μA, a decrease in the post-stimulation power spectra is observed (Fig. 6A and fig. S8). We believe that, at these amplitudes, overstimulation of neurons can transiently drive them into a hyperpolarized state, eventually

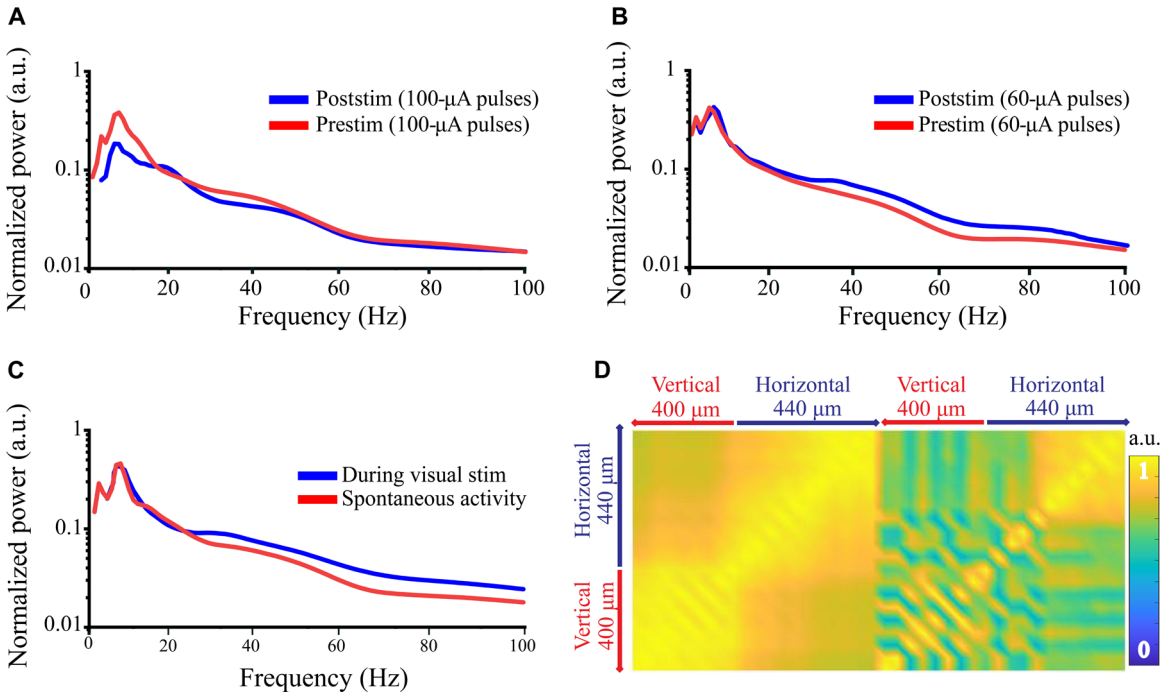

Fig. 6. LFP response during electrical and visual stimulation recorded at surface and depth by a 3D neural probe. (**A**) Power density before (red) and after stimulation (blue) at 0- to 100-Hz frequency band for 100-μA stimulation. a.u., arbitrary units. (**B**) Power density before (red) and after stimulation (blue) at 0- to 100-Hz frequency band for 60-μA stimulation. (**C**) Power density of spontaneous brain activity (red) and activity during visual stimulation (blue) at 0- to 100-Hz frequency band. (**D**) Pairwise coherence of surface and depth electrodes. Surface electrodes are marked by the blue arrow starting from stimulation side to the far end of the array (12 electrodes with a 40-μm pitch), and depth electrodes are marked by the red arrow implanted down to 400 μm (eight electrodes with a 50-μm pitch). The associated banding is obtained by generating pairwise coherence of every electrode pair throughout the array within 1- to 100-Hz frequency band. "1" represents the highest overlap in the frequency response, and "0" represents no overlap.

leading to a long-lasting depression (*39*, *40*). In addition, L1 neurons, which experience the highest current density, are primarily inhibitory GABAergic neurons (*30*). Activation of GABAergic neurons can contribute to inhibition of pyramidal neurons through cortical projections (*41*). Therefore, we limited our studies to 60-μA amplitude to avoid overstimulation. In response to 60-μA surface stimulation, however, an increase in the power spectra is observed in both the beta (20 to 30 Hz) and gamma bands (30 to 80 Hz) in Fig. 6B. Similarly, we also observe a significant increase in the gamma band (20 to 90 Hz) during visual stimulation, consistent with results shown by others (Fig. 6C and fig. S11) (*42*). Induced LFP modulation that overlaps with the spatiotemporal characteristics of both electrical and sensory stimulation demonstrates targeted stimulation.

To determine the spatial extent of the observed LFP variations recorded on the surface and at depth in response to 60-μA stimulation, we build a pairwise correlation map of the electrodes before and after the stimulation (Fig. 6D). We plot this map as a function of electrode distance from the depth shank, allowing us to correlate depth electrodes down to 400 μm with surface electrodes up to 440 μm away. The results show that prestimulation signals at the surface are most similar to the ones in superficial layers and the similarity exponentially decreases with cortical depth. This, along with the high spatial selectivity of the device, indicates the locality of the recorded LFP activity. Bipolar surface stimulation with 60-μA amplitude causes neurons in the vicinity of stimulation electrodes to go out of synchronization with the rest of the surrounding population. We observed this as a decrease in the coherence band between surface electrodes and those with depths beyond 300 μm. A similar reduction in the coherence band is noted on the surface at distances of more than 100 μm away from the stimulation electrode. This locality is consistent with current density measurements shown in Fig. 1D and the 3D neuropil response map for 2p imaging shown in Fig. 2C.

Effects of microstimulation on tissue and electrode integrity

In this work, successful stimulation of neural populations has been achieved with maximum current amplitude of 60 μA. This, however, leads to current densities in excess of 34000 μC/cm^2 which exceeds safety limits (typically 30 to 200 μC/cm^2) that have traditionally been observed for clinical macroelectrodes (*43*). These limits, however, differ for microelectrodes as current propagation follows a point source behavior and reaches high levels only at the immediate proximity of the electrode. It has been proposed that, in high current density zones near a microelectrode, the neural damage can only occur through electrochemical processes taking place at the electrode-electrolyte interface (*44*), which is minimal for PEDOT:PSS electrodes because of their non-Faradaic characteristics. To test both the potential tissue damage in a chronic use case and the robustness of the electrodes with extended use, we fabricate a set of nontransparent PEDOT:PSS electrodes at a diameter of 15 μm optimized for chronic use (Fig. 7A).

Long-term mechanical stability of thin-film PEDOT:PSS electrodes generally relies on the addition of a chemical cross linker, 3-glycidoxypropyltrimethoxysilane (GOPS) (*45*). Even with the presence of GOPS, it has been previously shown that PEDOT:PSS-coated

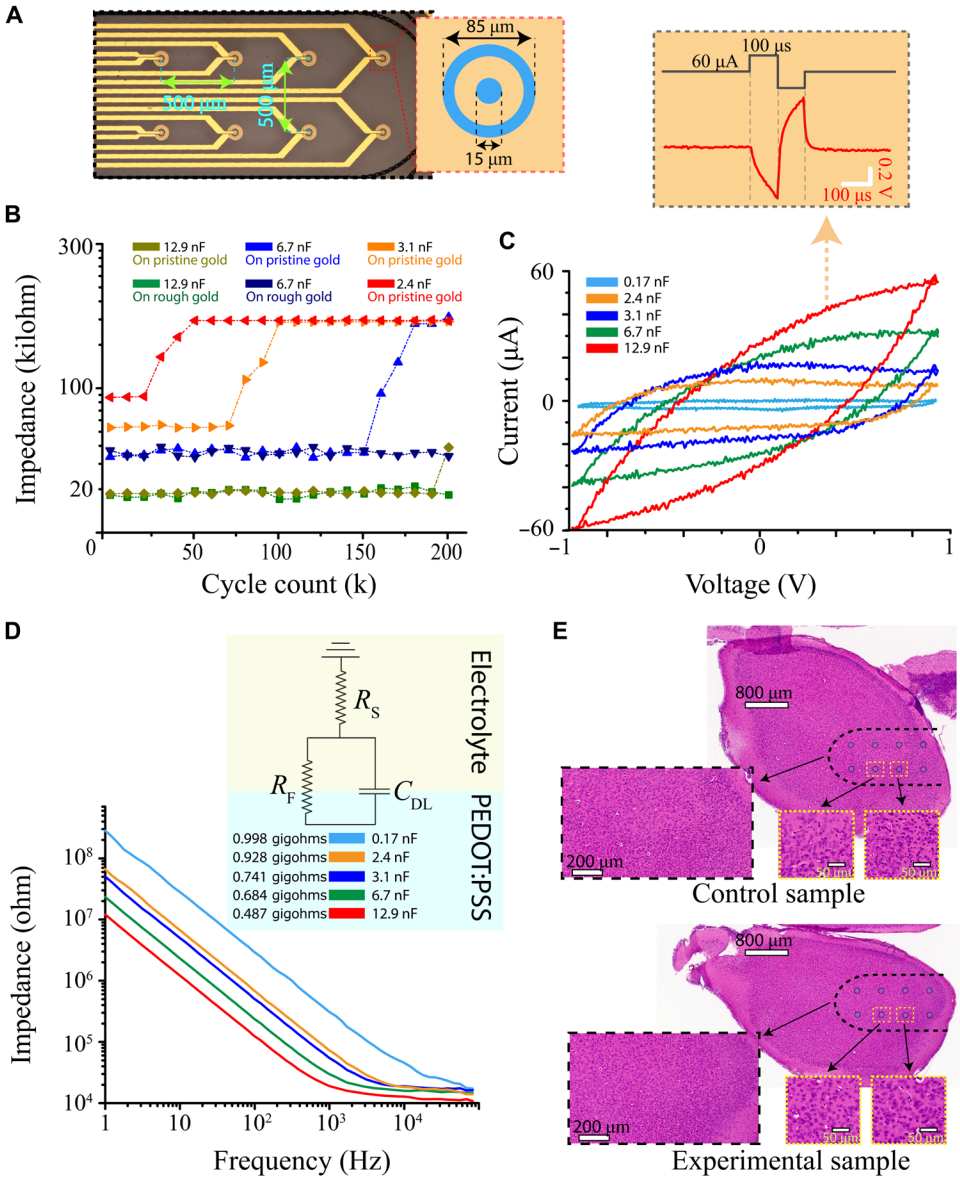

Fig. 7. Effects of microstimulation on tissue and electrode integrity. (**A**) A micrograph of the implanted surface array with eight electrodes spaced at a 500-µm pitch for better separation of postimplantation tissue damage per electrode. The inset illustrates a single electrode pair with a 15-µm cathode electrode surrounded by a ring electrode with 25-µm spacing. (**B**) Electrode impedance at 1 kHz as a function of applied pulse count for various PEDOT:PSS thickness values: 300, 400, and 850 nm and 1.5 µm, respectively. The 850-nm and 1.5-µm coatings are tested on both pristine and rough gold electrodes. Every value is averaged from eight electrodes located on the same array and acquired during in vivo tests after every 10,000 stimulation pulses. (**C**) Cyclic voltammetry (CV) curves of PEDOT:PSS electrodes as a function of coating thickness [bare gold and coating thicknesses as in (B)]. Inset illustrates the voltage transients recorded during stimulation with 12.9-nF electrode. (**D**) Impedance spectra of 15-µm electrodes as a function of coating thickness. Inset illustrates the equivalent R-R/C circuit at the electrolyte interface and capacitance and resistance values acquired by using it. (**E**) Histology results of implanted surface array after 200,000 stimulation pulses. (Horizontal sections) Top image illustrates results obtained from nonstimulated tissue. Bottom image illustrates the results obtained from hematoxylin and eosin (H&E) staining of brain sample stimulated with 200,000 pulses. Contours of the implanted arrays and location of individual electrodes are marked on the horizontal section. Zoomed-in (10× and 40×) versions of the implantation zone is placed within the brackets showing the H&E stained section of under the entire array (bottom left) and under two electrodes marked in orange (bottom right).

electrodes can fail in long-term applications because of coating delamination and cracking (*46*, *47*). To test these effects with 60-µA biphasic stimulation pulses, we fabricated a set of 15-µm-diameter electrodes with different coating thicknesses; therefore, different capacitance values with a GOPS concentration of 1.2% by weight. In addition, we roughen the gold surface (see Materials and Methods) to enhance adhesion by increasing the surface area and inducing hydroxyl groups at the substrate surface as shown in fig. S12 (*48*).

We plot impedance (at 1 kHz) spectra for each thickness averaged by eight electrodes as a function of stimulation pulse count (Fig. 7B). We observe that thin-coated electrodes (<300 nm) fail at relatively low cycle counts (<25,000), which is a consequence of the lower

capacitance of these films (fig. S13). Corresponding SEM images show strong buckling and delamination of coating, especially at the center of the electrode where current density is highest. Enhanced electrode stability is apparent, however, as coating thickness is increased, which is consistent with previous publications (*49*). We also show that this stability is enhanced further with roughened gold electrodes while keeping the coating thickness the same. This validates that delamination is a major factor in electrode failure. Alternative strategies to improve adhesion such as using sputtered IrO_x or P(EDOT-NH2) as an adhesion layer can also be used to enhance this further based on the requirement of the application (*49*, *50*).

One of the primary reasons for induced tissue damage during stimulation is electroporation due to the large voltage levels reached on traditional low-capacitance metal electrodes (*50*). Voltage values exceeding 1 V can also induce hydrolysis and damage nearby neurons through irreversible chemical reactions producing toxic by-products and changes in pH. PEDOT:PSS electrodes, however, owing to their high capacitance, result in much lower voltage operation. We show that PEDOT:PSS electrodes with capacitance values exceeding 10 nF allows sub–1-V operation for 60-μA stimulation pulses (Fig. 7C).

In addition to electroporation, Joule heating can also result in tissue damage. From the measured impedance spectra for the electrode, we extract the equivalent circuit model for the electrode shown in Fig. 7D, where R_S is the solution resistance, R_F is the Faradaic leakage, and C_{DL} is the double-layer capacitance. Typical Faradaic leakage current for these electrodes at the stimulation frequencies used here (>5 kHz) are in the picoampere range; Joule heating is therefore dominated by displacement currents flowing through the tissue. The resulting temperature change is given by (*51*)

$$\Delta T = \frac{\frac{1}{\sigma}\varphi^2 \tau}{pc}$$

where σ is the tissue conductivity (0.3300 S/m), φ is the current density, τ is the pulse duration (biphasic, 200 μs), p is the tissue density (1 kg/liter), and c is the heat capacity of the brain (3630 J/kg per °C). Using the current values measured in Fig. 1D, we calculate that the heating does not to exceed 37.16°C at a distance of 20 μm from the electrode surface (fig. S14). In immediate proximity of the electrodes, however, this high current density may produce temperatures over 38°C. We do not believe that these temperatures are reached in practice because of the heat sinking provided by electrodes themselves, combined with the thermal conductivity of the tissue and blood perfusion. To investigate any potential tissue damage, we implant electrode arrays shown in Fig. 7A with cathode capacitance of 12.9 nF. We apply 60-μA bipolar stimulation pulses with the low duty cycle (5 Hz) that is commonly used for responsive or scheduled stimulation paradigms (*43*) to be able to keep excitatory neurotoxicity at a minimum and allow heat dissipation between pulses. A total of 50,000 stimulation pulses are applied per day for 4 days. Upon completion of the chronic stimulation study, tissue is extracted for histological analysis (see Materials and Methods). The 20-μm-thick horizontal sections of tissue do not show any apparent change at the stimulation sites when compared to control samples (Fig. 7E).

DISCUSSION

Here, we validate direct bidirectional communication with L2/L3 pyramidal neurons using high-density microelectrode arrays. Using bipolar stimulation of axonal structures, which we demonstrate to be the input of surface stimulation, we show lateral confinement for stimulation that is defined by electrode size and spacing down to 15 and 25 μm, respectively. At these smallest electrode sizes, we show that neuronal response can be tuned spatially with current amplitude between 45 and 60 μA to depths of 220 and 280 μm, respectively. We also show electrical stimulation–induced gamma band modulation in V1, which overlaps the spatiotemporal scales of visual stimulation. Within the stimulated tissue, we validate that the stimulating microelectrodes can also record the corresponding activity of both individual pyramidal neurons and larger somatic groups at depths of 160 to 270 μm. While this work used a network of only 60 electrodes to investigate these limits of stimulation, the device structure is easily scalable to larger surface arrays either with passive electrode arrays wired back to electronics (*52*) or with active complementary metal-oxide semiconductor substrates (*53*), which can be rendered flexible through thinning. In the visual cortex, this may allow the targeting of particular microcircuits that correspond to detailed characteristics of visual stimulation, such as orientation, color, and direction.

The ultrathin nature of these thin film devices increases their biocompatibility. It is well known that thin-film parylene can conform to the curvilinear structure of the brain and improve electrical coupling. In this work, we have enhanced this further with subdural implantation. Subdural stimulation produces far more reliable stimulation responses from animal to animal (>90%) than those observed with dura removal under the same stimulation conditions (~30%). In addition, experiments that require very consistent effects on the same group of cells require exceptional electrode stability and tissue device sealing that is difficult to achieve with rigid electrodes. By allowing the parylene films to settle on the tissue fully and by bonding the "neck" of the probe to the skull without any tension applied to the active area, the probe is allowed to move freely with the brain tissue, keeping it in perfect relative positioning even during awake experiments.

High current densities on the superficial layer of brain lead to overstimulation, leading to cortical depression and overstimulation toxicity. In addition, it may lead to high temperature changes on proximity of the electrode surface and faster electrode degradation. Therefore, we minimize the current output of the array to a maximum level of 60 μA for selective activation of L2/L3 excitatory pyramidal neurons. The current propagation from the surface of the brain follows a semi-circular path. At large distances above several hundred micrometers where axonal structures are located, electrode size plays a small role in current density distribution (*54*). This allows tuning the size of the stimulation electrode, which can potentially decrease the charge injection in the immediate vicinity of electrodes, while keeping the current density in the L2/L3 constant for deeper range stimulation. This way, axons at L4 can be accessed, which constitutes the main sensory input layer in V1 (*55*). In addition, all of the work presented here was conducted using mice. Larger animal models such as cats or monkeys have been shown to have much longer axonal structures in the range of several hundred micrometers to millimeters, which can lead to higher sparsity for somatic activation. Extending the research to these models with different anatomical structures would be beneficial to obtain similar response maps and define the minimum resolution of stimulation for different models.

In summary, we have demonstrated targeted and focused stimulation using a minimally invasive electrode array on superficial layers

of the cortex is possible. Clinical applications of superficial stimulation usually rely on much higher stimulation levels, resulting in a much larger field of stimulation that lacks specificity. Engineered shaping of the spatial profiles of stimulation by dense electrode structures in close electrical contact with the pial surfaces allows for the activation of small population of spatially localized neurons.

MATERIALS AND METHODS

Material preparation

GOPS, 4-dodecylbenzenesulfonic acid (DBSA), 3-(trimethoxysilyl) propyl methacrylate (A-174 silane), ethylene glycol (EG), H_2SO_4, GABA, and ZD7288 were purchased from Sigma-Aldrich; and PEDOT:PSS (Clevios PH1000) was purchased from Heraeus. Shipley photoresist AZ9260 (positive photoresist) and AZ400K and AZ300MIF (metal ion free) developers were acquired from Micro-Chemicals, Merck. As an electrode interface material, PEDOT:PSS aqueous dispersions were prepared and mixed with GOPS [1.2 weight (wt) %] for enhanced stability during stimulation, DBSA (0.1 wt %), and EG (4.9 wt %). Aquasonic ultrasound gel, used as an immersion material, was purchased from Parker Laboratories. For control experiments, GABA and ZD7288 were purchased from Sigma-Aldrich.

Device fabrication

For transparent electrodes, a three-inch fused silica wafer was coated with 2 μm of parylene C using chemical vapor deposition in a SCS Parylene Coater. For liftoff processing, a 1-μm-thick film of LOR 3A and 300-nm-thick film of S1811 was spin-coated on the parylene substrate and cured at 130°C for 5 min and 110°C for 1 min, respectively. The wafer was exposed to ultraviolet light using a Suss MA6 Mask Aligner and developed with AZ300MIF developer for 25 s. A 10-nm-thick Ti adhesion layer, followed by a 100-nm-thick Au layer, was deposited on the patterned photoresist by using an Angstrom EvoVac Multi-Process Evaporator. The resultant wafers were soaked in Remover PG (Kayaku Advanced Materials Inc., Westborough, MA) for 12 hours for liftoff. The PEDOT:PSS dispersion was spin-coated on the wafer and baked at 115°C for 30 min. A film of PMMA495, a protective layer to prevent exposure of PEDOT:PSS to developer in subsequent photoresist development steps, was spin-coated at 2000 rpm and cured at 130°C for 5 min. A 1-μm-thick film of Shipley S1811 photoresist is coated, cured, and exposed to act as an etch mask for PEDOT:PSS patterning. A dry etch process is performed with a plasma-reactive ion etcher [100 W; 30 standard cubic centimeter per minute (SCCM) O_2 and 2 SCCM SF_6; Oxford Plasmalab 80], and residual photoresist is rinsed off using Remover PG. To enhance the conductivity of PEDOT:PSS, 250 μl of H_2SO_4 solution was dropped onto active area and baked at 160°C until it completely dries. After this, the PEDOT:PSS was rinsed off with deionized water multiple times and baked at 110°C for 10 min to dehydrate. Before coating with the top layer insulation, a layer of photoresist was deposited on the PEDOT:PSS to protect it during the final etching required to define the electrodes. A layer of LOR 3A and a 4-μm-thick layer of SU8 3005 were coated, cured, and developed. A second 2-μm-thick parylene C film was deposited using chemical vapor deposition using A-174 silane as an adhesion promoter. A final layer of parylene C was deposited following a spin-coating step of soap solution diluted to 1% concentration in deionized water. This layer acts as a sacrificial layer to clean off the photoresist after the final etch step, such that residues do not stick to the PEDOT:PSS and decrease transparency. A 8-μm-thick layer of AZ9260 was spin-coated at 3000 revolutions per minute (rpm), baked at 115°C for 2 min, exposed using a Suss MA6 Mask Aligner and developed with AZ400K developer. A second dry etch process is performed in a plasma-reactive ion etcher (180 W; 60 SCCM O_2 and 2 SCCM SF_6; Oxford Plasmalab 80). The sacrificial layer of parylene C was peeled off to remove any AZ9260 residues. Patterned LOR 3A and SU8 films covering the electrodes during the etching step were removed with exposure to Remover PG for 1 min. The contour of the surface array and shanks were patterned by using an IPG Photonics excimer laser cutter. Exposed pads were sputtered the 4-μm-thick copper using at a power of 420 W for 1800 s in an AJA Orion Sputtering System. This copper buildup is necessary to make the pads level the pads with the surrounding passivation, which is necessary for electrical bonding. Last, the parylene devices were bonded to a custom-made printed circuit board for connection to the recording and stimulation electronics using a FINEPLACER Lambda (Finetech, Berlin, Germany) and anisotropic conductive paste (3 M) at 160°C and 50 kPa for 30 s.

Nontransparent electrodes for chronic studies were fabricated by patterning gold on a parylene substrate following the methods described above. For multilayer structures used for combined surface and depth probes, a second 500-nm parylene layer was coated as a spacer between two layers of gold interconnects. As insulation, 2-μm-thick parylene C film was deposited using chemical vapor deposition using A-174 silane as an adhesion promoter. A final layer of parylene C was deposited following a spin-coating step of soap solution diluted to 1% concentration in deionized water. A 8-μm-thick layer of AZ9260 was patterned as an etch mask, and using plasma-reactive ion etcher, parylene was etched until gold layers. To promote adhesion of the PEDOT:PSS, the gold surface is roughened. First samples were deposited with an additional 200 nm of gold and then etched using a plasma-reactive ion etcher (160 W; 60 SCCM SF_6 between 30 and 270 s; Oxford Plasmalab 80). Immediately after etching, an aqueous dispersion of PEDOT:PSS was spin-coated at thickness values between 30 and 1500 nm, and the sacrificial layer of parylene was peeled off to complete PEDOT:PSS patterning. PEDOT:PSS thickness values were controlled by adjusting the spin speed between 1000 and 5000 rpm. For thicker coatings exceeding 200 nm, multiple spin coatings with 30 s of soft bake step at 110°C in-between was performed.

2p imaging

The Institutional Animal Care and Use Committee (IACUC) reviewed and approved protocols for Columbia University's program for the humane care and use of animals and inspected the animal facilities and investigator laboratories. Evaluation of the implanted devices was performed in compliance with Animal Welfare and Columbia's IACUC regulations under approved IACUC protocol AC-AAAR4441 (development of high-density, implantable recording, imaging, and stimulating arrays) between 2018 and 2020 and AC-AABE5554 (development of high-density, implantable recording, imaging, and stimulating arrays) between 2020 and 2022. A mouse pair with strain Vglut1-IRES2-Cre-D and strain Ai148(TIT2L-GC6f-ICL-tTA2)-D (or Ai148D) were mated to generate offspring having GCaMP6f expression and tTA2 expression. Pups were implanted at a minimum age of six months to ensure an enhanced thickness of dura mater suitable with the implantation protocol in Fig. 1C. For electrophysiology experiments, wild-type (WT) mice

were purchased from the Jackson Laboratory with strain 000664 (15 to 18 weeks old). For implantation, the transgenic or WT mouse was anesthetized using isoflurane with an induction level of 3% and driven by an oxygen flow at the rate of 2 liter/min. Upon induction of anesthesia, the animal was removed from the induction chamber and placed on a stereotactic frame, which is attached to a nose cone to maintain a steady flow of isoflurane. The body temperature of the mouse was controlled using a feedback-regulated rodent warmer (ATC-2000) pad set at 32°C. A total of 0.2 ml of bupivacaine was injected subcutaneously under the scalp before removal. A custom-designed cathodized titanium headplate was fixed on the exposed skull using dental cement to achieve head fixing for imaging. The skull over V1 was drilled in a 3-mm-diameter circular shape by a dental drill and gently removed. Dura mater was incised using a dura hook. The surface electrode array was laminated on the brain and a coverslip was placed on it to act as an imaging window. Coverslip was affixed with dental cement on the sides. Carprofen (2 mg/kg concentration) was intraperitoneally injected to the abdominal area of the animal. The animal was placed on a battery powered heat pad and inspected until it regains consciousness. Upon recovery, the animal is transferred to the microscope area and head fixed to a metallic arm to keep it steady during imaging.

For 2p imaging, an excitation laser (Chameleon Vision) was used to provide output with a wavelength of 920 nm and output power of 30 mW. The output is collected by a photomultiplier tube (4745T GaAsP) after a set of dichroic mirrors and band-pass filters within the range of 420 and 500 nm. Images were recorded using a Nikon ×16 objective immersed in ultrasound gel. ScanImage software (Vidrio Technologies LLC, Ashburn, VA) is used to acquire the data at 30 Hz in resonance imaging mode. The calcium imaging data sequences were preprocessed with the Suite2p pipeline for trace extraction. Changes in fluorescence for somatic activity were calculated subtracting from each region of interest signal surrounding neuropil signal scaled by a factor of 0.7. Calcium events at the time of stimulation are carried out with a peak analysis function. By averaging 30 s of calcium traces of the same pixel, background activity is obtained. Calculated $\Delta F/F$ is used for event analysis, and neuropil image maps displayed in the figures.

Visual stimulation experiments

For visual stimulation experiments, mice were first implanted with headplates and adapted to head restraint through daily training sessions. After 1 week of training, device implantation was conducted as described above. Upon a week of recovery, animals were head-fixed on a wheel and visual stimulation was conducted by drifting sinusoidal gratings (at high contrast, spatial frequency of 2 cycles per degree, temporal frequency of 4 Hz) within a circular patch with a diameter to cover a 3° visual angle, the entire visual field of all the recording sites. Mean luminance of the stimulus patch and that of the rest of the screen were kept at the same level. The stimulus in each condition was presented for 5 s and repeated 10 times.

Electrophysiology recordings and analysis

Extracellular electrophysiology data were acquired, and stimulation pulses were applied using an Intan RHS2000 system with a sampling rate of 30 kHz. Both electrophysiology and imaging acquisition systems were driven by a LabVIEW-controlled data acquisition board (National Instruments USB-6343) to achieve synchronization of stimulation pulses and recording/imaging times. Electrophysiology data were analyzed separately for spike and LFP information. The data were acquired over the range of 0.15 Hz to 7 kHz and Butterworth-filtered between 300 Hz and 4 kHz for spike detection. The LFP bands were analyzed with a custom-written MATLAB code to extract LFP time frequency information using wavelet transformations (Gabor) and LFP coherence at different frequency bands. Single neuronal spikes were sorted using Kilosort 2.5 and plotted with custom MATLAB code to visualize waveforms at the times of stimulation. Pre- and post-stimulation LFP modulation and spiking rates were measured at two 2-s windows, one preceding the stimulation pulse and one following the stimulation artifact.

Current density measurements

Borosilicate glass pipettes (1 to 0.5 mm^2) were pulled with an inner diameter of 500 nm using a Sutter Instrument model P-97. They were filled with a 3 M KCl solution and integrated with Axon MultiClamp and Axon Digidata 1550 modules for data acquisition. Pipettes were implanted using a Sensapex uMp zero drift manipulator. Current values were recorded using the pCLAMP 10 software suite (Molecular Devices LLC, San Jose, CA). To be able to get an accurate 2D map of charge density, for each stimulation pulse, the micropipette is repositioned axially (by varying the depth of penetration with 20-μm steps down to 500 μm below the pial surface), and for each axial position, a selection of electrodes at various lateral positions with a pitch of 40 μm are activated sequentially. To obtain current values, voltage values are acquired in current-clamp mode with $I = 0$. Measured tissue resistance (at DC) at the point of current value measurement with respect to the reference (that is grounded) is used to estimate the current value. To increase the accuracy of this estimation, current values are averaged for each point from five different experiments with variations in the range of 20%.

Drug delivery

A 3-mm-thick coverslip was placed on a 2-inch wafer using Crystalbond 509 Clear. A 6-μm-thick layer of parylene C was deposited following a spin-coating step of soap solution diluted to 5% concentration in deionized water. A 6-μm-thick layer of AZ9260 was spin-coated at 5000 rpm, baked at 115°C for 2 min, exposed using a Suss MA6 Mask Aligner, and developed with AZ400K developer. A dry etch process was performed with a plasma-reactive ion etching (180 W; 60 SCCM O_2 and 2 SCCM SF_6; Oxford Plasmalab 80). The excess AZ9260 residuals were rinsed off using Remover PG. A PDMS membrane was spin-coated at 1000 rpm for 30 s to achieve a thickness of 20 μm and partially cured at 80°C for 20 s to minimize polymerization. A PDMS prepolymer with high liquidity was patterned by peeling away the sacrificial parylene C. The samples were then baked at 200°C for 5 min to form the PDMS fluidic channel. Upon implantation of the final device in the brain, a 10-μl Hamilton syringe mounted on a SMARTouch microsyringe pump (World Precision Instruments, Sarasota, FL) was used to inject GABA solution inside the channel through an inlet on the coverslip.

Device characterization

Impedance spectra of the electrodes were measured using an Autolab Potentiostat (Metrohm Autolab, Utrecht, Netherlands) equipped with a frequency-response-analysis module. A commercially available Ag/AgCl electrode and a platinum mesh (30 mm by 30 mm) immobilized inside the bath were used as the reference and counter-electrodes, respectively. The counter-electrode was kept sufficiently

large to minimize its impedance contribution to the measured data. The applied AC voltage of 0.01-V amplitude was applied, and the corresponding DC open-circuit potential against the reference electrode was acquired. For cyclic voltammetry, the voltage ranged from −1 to 1 V, and the scan rate was 5000 V/s with steps of 0.002 V. Two scans were used to stabilize the shape of the voltammogram.

Histology tests

For evaluating the tissue damage for subdural implantation and high current stimulation, two separate experiments were performed. For device compatibility test, for control and experimental groups, cranial window opening and dura incision were performed as described above. For experimental groups, devices were implanted. For control groups, no device was implanted. For both cases, mice were kept for 1 month before histology tests. For stimulation integrity tests, devices were implanted for both control and experimental groups. Stimulation pulses with 1-s stimulation envelopes (biphasic 60 μA, 100 μs per phase pulses at 5 Hz) with 4-s interval were applied by devices implanted in the experimental groups. Devices at the control group were not used for stimulation. Stimulation was initiated on day 8 and repeated for 4 days (50,000 pulses a day). Both control and experimental devices were kept implanted until day 20th.

Upon completion of chronic tests, mice were anesthetized using isoflurane with an induction level of 3% and driven by an oxygen flow at the rate of 2 liter/min. Upon induction of anesthesia, the mouse was decapitated, and brain was extracted. Extracted brain was trimmed until the visual cortex using a Compresstome VF 310-0Z and placed in 10% formalin for 24 hours. For tissue reaction experiments, the cortical tissues from both implanted and control experiments were placed in paraffin blocks and sectioned coronally. For stimulation damage tests, tissues were sectioned horizontally. To achieve better comparison, control and experimental samples were processed together. Sections were collected and processed for hematoxylin and eosin (H&E) staining. Images of H&E-stained tissue sections were scanned using an Aperio LV1 slide scanner at ×40 magnification. Sectioning of paraffin blocks, staining, and scanning was conducted by Columbia University's Molecular Pathology Core Facility (www.cancer.columbia.edu/research/shared-resources/molecular-pathology).

SUPPLEMENTARY MATERIALS

Supplementary material for this article is available at https://science.org/doi/10.1126/sciadv.abq6354

View/request a protocol for this paper from *Bio-protocol*.

REFERENCES AND NOTES

1. J. M. Hu, M. Z. Qian, H. Tanigawa, X. M. Song, A. W. Roe, Focal electrical stimulation of cortical functional networks. *Cereb. Cortex* **30**, 5532–5543 (2020).
2. E. J. Tehovnik, A. S. Tolias, F. Sultan, W. M. Slocum, N. K. Logothetis, Direct and indirect activation of cortical neurons by electrical microstimulation. *J. Neurophysiol.* **96**, 512–521 (2006).
3. G. S. Brindley, W. S. Lewin, The sensations produced by electrical stimulation of the visual cortex. *J. Physiol.* **196**, 479–493 (1968).
4. W. H. Dobelle, M. G. Mladejovsky, Phosphenes produced by electrical stimulation of human occipital cortex, and their application to the development of a prosthesis for the blind. *J. Physiol.* **243**, 553–576 (1974).
5. H. Asanuma, H. Sakata, Functional organization of a cortical efferent system examined with focal depth stimulation in cats. *J. Neurophysiol.* **30**, 35–54 (1967).
6. S. D. Stoney Jr., W. D. Thompson, H. Asanuma, Excitation of pyramidal tract cells by intracortical microstimulation: Effective extent of stimulating current. *J. Neurophysiol.* **31**, 659–669 (1968).
7. M. H. Histed, V. Bonin, R. C. Reid, Direct activation of sparse, distributed populations of cortical neurons by electrical microstimulation. *Neuron* **63**, 508–522 (2009).
8. E. J. Tehovnik, W. M. Slocum, Two-photon imaging and the activation of cortical neurons. *Neuroscience* **245**, 12–25 (2013).
9. A. S. Tolias, F. Sultan, M. Augath, A. Oeltermann, E. J. Tehovnik, P. H. Schiller, N. K. Logothetis, Mapping cortical activity elicited with electrical microstimulation using fMRI in the macaque. *Neuron* **48**, 901–911 (2005).
10. W. A. Catterall, Localization of sodium channels in cultured neural cells. *J. Neurosci.* **1**, 777–783 (1981).
11. D. C. Bradley, P. R. Troyk, J. A. Berg, M. Bak, S. Cogan, R. Erickson, C. Kufta, M. Mascaro, D. McCreery, E. M. Schmidt, V. L. Towle, H. Xu, Visuotopic mapping through a multichannel stimulating implant in primate V1. *J. Neurophysiol.* **93**, 1659–1670 (2005).
12. T. S. Davis, R. A. Parker, P. A. House, E. Bagley, S. Wendelken, R. A. Normann, B. Greger, Spatial and temporal characteristics of V1 microstimulation during chronic implantation of a microelectrode array in a behaving macaque. *J. Neural Eng.* **9**, 065003 (2012).
13. K. Torab, T. S. Davis, D. J. Warren, P. A. House, R. A. Normann, B. Greger, Multiple factors may influence the performance of a visual prosthesis based on intracortical microstimulation: Nonhuman primate behavioural experimentation. *J. Neural Eng.* **8**, 035001 (2011).
14. V. S. Polikov, P. A. Tresco, W. M. Reichert, Response of brain tissue to chronically implanted neural electrodes. *J. Neurosci. Methods* **148**, 1–18 (2005).
15. P. K. Campbell, K. E. Jones, R. J. Huber, K. W. Horch, R. A. Normann, A silicon-based, three-dimensional neural interface: Manufacturing processes for an intracortical electrode array. *IEEE Trans. Biomed. Eng.* **38**, 758–768 (1991).
16. D. Khodagholy, J. N. Gelinas, T. Thesen, W. Doyle, O. Devinsky, G. G. Malliaras, G. Buzsáki, NeuroGrid: Recording action potentials from the surface of the brain. *Nat. Neurosci.* **18**, 310–315 (2015).
17. J. Viventi, D. H. Kim, L. Vigeland, E. S. Frechette, J. A. Blanco, Y. S. Kim, A. E. Avrin, V. R. Tiruvadi, S. W. Hwang, A. C. Vanleer, D. F. Wulsin, K. Davis, C. E. Gelber, L. Palmer, J. van der Spiegel, J. Wu, J. Xiao, Y. Huang, D. Contreras, J. A. Rogers, B. Litt, Flexible, foldable, actively multiplexed, high-density electrode array for mapping brain activity in vivo. *Nat. Neurosci.* **14**, 1599–1605 (2011).
18. I. R. Minev, P. Musienko, A. Hirsch, Q. Barraud, N. Wenger, E. M. Moraud, J. Gandar, M. Capogrosso, T. Milekovic, L. Asboth, R. F. Torres, N. Vachicouras, Q. Liu, N. Pavlova, S. Duis, A. Larmagnac, J. Vörös, S. Micera, Z. Suo, G. Courtine, S. P. Lacour, Electronic dura mater for long-term multimodal neural interfaces. *Science* **347**, 159–163 (2015).
19. M. S. Humayun, Intraocular retinal prosthesis. *Trans. Am. Ophthalmol. Soc.* **99**, 271–300 (2001).
20. M. B. Voigt, P. Hubka, A. Kral, Intracortical microstimulation differentially activates cortical layers based on stimulation depth. *Brain Stimul.* **10**, 684–694 (2017).
21. E. J. Tehovnik, W. M. Slocum, S. M. Smirnakis, A. S. Tolias, Microstimulation of visual cortex to restore vision. *Prog. Brain Res.* **175**, 347–375 (2009).
22. C. M. Proctor, J. Rivnay, G. G. Malliaras, Understanding volumetric capacitance in conducting polymers. *J. Polym. Sci. B Polym. Phys.* **54**, 1433–1436 (2016).
23. A. M. Thomson, C. Lamy, Functional maps of neocortical local circuitry. *Front. Neurosci.* **1**, 19–42 (2007).
24. N. Kim, S. Kee, S. H. Lee, B. H. Lee, Y. H. Kahng, Y. R. Jo, B. J. Kim, K. Lee, Highly conductive PEDOT:PSS nanofibrils induced by solution-processed crystallization. *Adv. Mater.* **26**, 2268–2272 (2014).
25. T. Deneux, A. Kaszas, G. Szalay, G. Katona, T. Lakner, A. Grinvald, B. Rozsa, I. Vanzetta, Accurate spike estimation from noisy calcium signals for ultrafast three-dimensional imaging of large neuronal populations in vivo. *Nat. Commun.* **7**, 12190 (2016).
26. M. Pachitariu, C. Stringer, M. Dipoppa, S. Schröder, L. F. Rossi, H. Dalgleish, M. Carandini, K. Harris, Suite2p: Beyond 10,000 neurons with standard two-photon microscopy. *bioRxiv* 10.1101/061507 , (2016).
27. J. N. D. Kerr, D. Greenberg, F. Helmchen, Imaging input and output of neocortical networks in vivo. *Proc. Natl. Acad. Sci. U.S.A.* **102**, 14063–14068 (2005).
28. J. Tong, C. A. Simmons, Y. Sun, Precision patterning of PDMS membranes and applications. *J. Micromech. Microeng.* **18**, 037004 (2008).
29. C. M. Proctor, I. Uguz, A. Slezia, V. Curto, S. Inal, A. Williamson, G. G. Malliaras, An electrocorticography device with an integrated microfluidic ion pump for simultaneous neural recording and electrophoretic drug delivery in vivo. *Adv. Biosyst.* **3**, 1800270 (2019).
30. S. Muralidhar, Y. Wang, H. Markram, Synaptic and cellular organization of layer 1 of the developing rat somatosensory cortex. *Front. Neuroanat.* **7**, 52 (2014).
31. M. V. Jones, G. L. Westbrook, Desensitized states prolong GABAA channel responses to brief agonist pulses. *Neuron* **15**, 181–191 (1995).
32. M. T. Harnett, J. C. Magee, S. R. Williams, Distribution and function of HCN channels in the apical dendritic tuft of neocortical pyramidal neurons. *J. Neurosci.* **35**, 1024–1037 (2015).
33. J. A. Boychuk, J. S. Farrell, L. A. Palmer, A. C. Singleton, Q. J. Pittman, G. C. Teskey, HCN channels segregate stimulation-evoked movement responses in neocortex and allow for coordinated forelimb movements in rodents. *J. Physiol.* **595**, 247–263 (2017).

34. G. Buzsáki, C. A. Anastassiou, C. Koch, The origin of extracellular fields and currents—EEG, ECoG, LFP and spikes. *Nat. Rev. Neurosci.* **13**, 407–420 (2012).
35. N. Maurice, A. M. Thierry, J. Glowinski, J. M. Deniau, Spontaneous and evoked activity of substantia nigra pars reticulata neurons during high-frequency stimulation of the subthalamic nucleus. *J. Neurosci.* **23**, 9929–9936 (2003).
36. M. Pachitariu, N. Steinmetz, S. Kadir, M. Carandini, H. Kenneth D, Kilosort: Realtime spike-sorting for extracellular electrophysiology with hundreds of channels. *bioRxiv* 10.1101/061481 (2016).
37. W. S. Konerding, U. P. Froriep, A. Kral, P. Baumhoff, New thin-film surface electrode array enables brain mapping with high spatial acuity in rodents. *Sci. Rep.* **8**, 3825 (2018).
38. S. Katzner, I. Nauhaus, A. Benucci, V. Bonin, D. L. Ringach, M. Carandini, Local origin of field potentials in visual cortex. *Neuron* **61**, 35–41 (2009).
39. N. K. Logothetis, M. Augath, Y. Murayama, A. Rauch, F. Sultan, J. Goense, A. Oeltermann, H. Merkle, The effects of electrical microstimulation on cortical signal propagation. *Nat. Neurosci.* **13**, 1283–1291 (2010).
40. S. Butovas, C. Schwarz, Spatiotemporal effects of microstimulation in rat neocortex: A parametric study using multielectrode recordings. *J. Neurophysiol.* **90**, 3024–3039 (2003).
41. R. Tremblay, S. Lee, B. Rudy, GABAergic interneurons in the neocortex: From cellular properties to circuits. *Neuron* **91**, 260–292 (2016).
42. R. Land, G. Engler, A. Kral, A. K. Engel, Response properties of local field potentials and multiunit activity in the mouse visual cortex. *Neuroscience* **254**, 141–151 (2013).
43. S. F. Cogan, K. A. Ludwig, C. G. Welle, P. Takmakov, Tissue damage thresholds during therapeutic electrical stimulation. *J. Neural Eng.* **13**, 021001 (2016).
44. C. C. McIntyre, W. M. Grill, Finite element analysis of the current-density and electric field generated by metal microelectrodes. *Annals Biomed. Eng.* **29**, 227–235 (2001).
45. M. ElMahmoudy, S. Inal, A. Charrier, I. Uguz, G. G. Malliaras, S. Sanaur, Tailoring the electrochemical and mechanical properties of PEDOT:PSS films for bioelectronics. *Macromol. Mater. Eng.* **302**, 1600497 (2017).
46. X. T. Cui, D. D. Zhou, Poly (3,4-ethylenedioxythiophene) for chronic neural stimulation. *IEEE Trans. Neural Syst. Rehabil Eng.* **15**, 502–508 (2007).
47. M. Ganji, A. Tanaka, V. Gilja, E. Halgren, S. A. Dayeh, Scaling effects on the electrochemical stimulation performance of Au, Pt, and PEDOT:PSS electrocorticography arrays. *Adv. Funct. Mater.* **27**, 1703019 (2017).
48. A. S. Pranti, A. Schander, A. Bödecker, W. Lang, PEDOT: PSS coating on gold microelectrodes with excellent stability and high charge injection capacity for chronic neural interfaces. *Sens. Actuat. B Chem.* **275**, 382–393 (2018).
49. G. Dijk, H. J. Ruigrok, R. P. O'Connor, Influence of PEDOT:PSS coating thickness on the performance of stimulation electrodes. *Adv. Mater. Interfaces* **7**, 2000675 (2020).
50. A. Butterwick, A. Vankov, P. Huie, Y. Freyvert, D. Palanker, Tissue damage by pulsed electrical stimulation. *IEEE Trans. Biomed. Eng.* **54**, 2261–2267 (2007).
51. M. M. Stecker, T. Patterson, B. L. Netherton, Mechanisms of electrode induced injury. Part 1: Theory. *Am. J. Electroneurodiagnostic Technol.* **46**, 315–342 (2006).
52. Y. Tchoe, A. M. Bourhis, D. R. Cleary, B. Stedelin, J. Lee, K. J. Tonsfeldt, E. C. Brown, D. A. Siler, A. C. Paulk, J. C. Yang, H. Oh, Y. G. Ro, K. Lee, S. M. Russman, M. Ganji, I. Galton, S. Ben-Haim, A. M. Raslan, S. A. Dayeh, Human brain mapping with multithousand-channel PtNRGrids resolves spatiotemporal dynamics. *Sci. Transl. Med.* **14**, eabj1441 (2022).
53. D. Tsai, D. Sawyer, A. Bradd, R. Yuste, K. L. Shepard, A very large-scale microelectrode array for cellular-resolution electrophysiology. *Nat. Commun.* **8**, 1802 (2017).
54. E. J. Tehovnik, Electrical stimulation of neural tissue to evoke behavioral responses. *J. Neurosci. Methods* **65**, 1–17 (1996).
55. H. Adesnik, W. Bruns, H. Taniguchi, Z. J. Huang, M. Scanziani, A neural circuit for spatial summation in visual cortex. *Nature* **490**, 226–231 (2012).

Acknowledgments: The device fabrication was performed at Columbia Nano Initiative (CNI) and CUNY Advanced Science Research Center (ASRC) cleanroom facilities. We thank R. Bruno and S. E. Benezra for many helpful discussions. **Funding:** This work was supported, in part, by the Defense Advanced Research Projects Agency (DARPA) under contract N66001-17-C-4002.
Author contributions: I.U. and K.L.S. designed the research. I.U. developed the probes, performed the research, and analyzed the data. I.U. and K.L.S. wrote the manuscript.
Competing interests: The authors declare that they have no competing interests. **Data and materials availability:** All data needed to evaluate the conclusions in the paper are present in the paper and/or the Supplementary Materials. Source files, additional data, and MATLAB codes used in this research to analyze electrophysiology data are uploaded on https://doi.org/10.5281/zenodo.6972414.

Submitted 25 April 2022
Accepted 7 September 2022
Published 19 October 2022
10.1126/sciadv.abq6354